Facile Determination of the Spectra of Unstable Electrode Products Using Simultaneous Fiber-Optic Chronoabsorptometry and Chronoamperometry

Michael J. Shaw,*,[†] Daniel L. Cranford,[†] Kenneth W. Rodgers,[†] James E. Eilers,[†] Bradley Noble,[‡] Adam J. Warhausen,[§] and George B. Richter-Addo[§]

[†]*Department of Chemistry, Box 1652, Southern Illinois University at Edwardsville, Edwardsville, Illinois 62026,* [‡]*Department of Electrical and Computer Engineering, Box 1801, Southern Illinois University at Edwardsville, Edwardsville, Illinois 62026, and* [§]*Department of Chemistry and Biochemistry, University of Oklahoma, 620 Parrington Oval, Norman, Oklahoma 73019*

A widely applicable fiber-optic UV−vis method to determine the spectra of in situ generated redox products and intermediates at or near an electrode surface is described mathematically and implemented experimentally. The quantitative spectral information obtained gives extinction coefficients (absorptivities) as a function of wavelength, requires no arbitrary subtraction of the spectrum of the starting material, and is relatively insensitive to path length and concentration during the spectroelectrochemical measurements. We demonstrate proof-of-concept of this methodology by reproducing the expected spectrum of the ferrocenium ion from electrooxidation of ferrocene in MeCN, and by reproducing the spectrum that reveals π-radical cation formation from the electrooxidation of (T(p-OMe)PP)Co(NO) ((T(p-OMe)PP = 5,10,15,20-tetra(p-methoxyphenyl)porphyrinato dianion). Importantly, we demonstrate its use for the facile detection of unstable redox products not previously detected by current spectroelectrochemical methods. We obtain, for the first time, the experimental UV−vis spectrum of the short-lived *fac*-[(dppe)Mn(CO)$_3$Br]$^+$ cation, a hitherto uncharacterized intermediate that forms during the archetypal redox-induced *fac*-to-*mer* isomerization of (dppe)Mn(CO)$_3$Br (dppe = diphenylphosphinoethane). Spectral features of the Mn-containing species have been verified by comparison to theoretical spectra calculated by time-dependent density functional theory methods.

Introduction

The accurate identification of redox products is an important goal in chemistry, and significant effort has been placed on the use of spectroelectrochemical methods to aid in this goal. Successful approaches have been reported for the generation and identification of short-lived redox products, and these include methods involving the use of optically transparent thin layer electrochemical (OTTLE) cells,[1] bulk electrolyses and sampling of aliquots of product solutions, and chemical generation of redox products using chemical redox reagents.[2] The use of OTTLE cells has revolutionized the field of spectroscopic identification of electrode products, and numerous advances have been achieved using

this methodology. For example, Heath and co-workers have utilized OTTLE cells to obtain spectral data for a number of intermediates generated from fullerenes,[3] alkynyl-bridged organometallics,[4] alkynyl-bridged porphyrin complexes,[5] coordination compounds with M-M multiple bonds,[6] and other systems.[7] These examples include high-quality determinations of extinction coefficients from chemical species in multiple oxidation states at low temperatures.[8] For some systems, detailed information about non-linear third-order optical properties are available from OTTLE studies.[9]

Commercial OTTLE cells for UV−vis spectroelectrochemistry are now readily available.[10] However, some limitations remain. For example, factors such as (i) inaccuracies in cell path length because of the presence of a metallic electrode grid and non-reproducible spacer length after multiple cell

*To whom correspondence should be addressed. E-mail: michsha@siue.edu.

(1) Hawkridge, F. M. In *Laboratory Techniques in Electroanalytical Chemistry*; Kissinger, P. T., Heineman, W. R., Eds.; Marcel Dekker, Inc.: New York, 1996, pp 280−289.

(2) Connelly, N. G.; Geiger, W. E. *Chem. Rev.* **1996**, *96*, 877–910.

(3) Heath, G. A.; Mcgrady, J. E.; Martin, R. L. *J. Chem. Soc., Chem. Commun.* **1992**, 1272–1274.

(4) Powell, C. E.; Cifuentes, M. P.; Morrall, J. P.; Stranger, R.; Humphrey, M. G.; Samoc, M.; Luther-Davies, B.; Heath, G. A. *J. Am. Chem. Soc.* **2003**, *125*, 602–610.

(5) Arnold, D. P.; Heath, G. A. *J. Am. Chem. Soc.* **1993**, *115*, 12197–12198.

(6) Heath, G. A.; Raptis, R. G. *J. Am. Chem. Soc.* **1993**, *115*, 3768–3769.

(7) Baldas, J.; Heath, G. A.; Macgregor, S. A.; Moock, K. H.; Nissen, S. C.; Raptis, R. G. *J. Chem. Soc., Dalton Trans.* **1998**, 2303–2314.

(8) Webster, R. D.; Heath, G. A.; Bond, A. M. *J. Chem. Soc., Dalton Trans.* **2001**, 3189–3195.

(9) Morrall, J. P.; Powell, C. E.; Stranger, R.; Cifuentes, M. P.; Humphrey, M. G.; Heath, G. A. *J. Organomet. Chem.* **2003**, *670*, 248–255.

(10) The cell is available from BASi, W. L., IN 47906.

assemblies, (ii) influence of thin-layer resistance on the accuracy of the applied potential and the resulting need to change the applied potential slowly (increasing the chance of decomposition of electrode products), and (iii) other problems such as non-reproducible results because of the non-trivial assembly (and leakage) of the cell for the inexperienced researcher, limit the easy use of these OTTLE cells.

A new spectroelectrochemical method that overcomes, in part, the problems normally associated with OTTLE cells was reported in 1996.[11] Here, the authors made use of a commercial fiber-optic infrared (IR) reflectance instrument to monitor the progress of low-temperature bulk electrolysis experiments, and used this method to generate and characterize reactive redox products in non-aqueous solvents.[11] A modification of this method was reported in which the mirror in the transmission head was replaced by a Pt disk electrode that served as a reflecting mirror, allowing for the IR spectral identification (by difference spectral analysis) of electrochemically generated redox products at the electrode surface on a typical cyclic voltammetry time scale.[12] This allowed for the collection of spectra at shorter reaction times than were possible during bulk electrolysis experiments (e.g., collection of spectra during a single cyclic voltammetry scan at scan rates up to 0.4 V/s),[13] and allowed a simple modification to collect spectra of reactive species generated at variable (low) temperature.[14,15] In using this modified method, however, information on the relationship between current passed and the build-up of electrode products was lost.

We have developed a new method to recover quantitative spectral information on redox products generated at electrode surfaces. Specifically, we used chronoamperometry and chronoabsorptometry simultaneously to recover quantitative spectral information on the build-up of redox products at or near the electrode surface. Using this method, we can obtain the UV−vis spectra of electrode products without the use of arbitrary spectral subtraction such as that commonly used in the manual generation of difference (product-minus-reactant) spectra. We use mathematics to unambiguously determine plots of absorptivity (ε, extinction coefficient) versus wavelength of the electrode product(s). This method allows us to spectrally characterize electrode products with half-lives of ∼0.3 s or longer. In this article, we demonstrate proof-of-concept for this relatively simple new method and use it to determine the spectral characteristics of a previously invoked but elusive electrogenerated intermediate along a complex reaction pathway. We show that this new method is general and applicable to a wide variety of chemical systems.

Experimental Section

All solvents were dried under appropriate conditions and freeze−pump−thaw degassed before use.[16,17] The supporting electrolyte NBu_4PF_6 was obtained from Acros Chemicals, and was recrystallized from boiling ethanol and dried at 100 °C before use. Ferrocene was obtained from Acros Chemicals and was sublimed before use. $Mn_2(CO)_{10}$ was obtained from Alfa-Aesar and used as received. Literature methods were used to prepare $H_2T(p\text{-OMe})PP$,[18] $(T(p\text{-OMe})PP)Co$,[19] $(T(p\text{-OMe})PP)Co(NO)$,[20] and $fac\text{-}(dppe)Mn(CO)_3Br$[21] ($T(p\text{-OMe})\text{-}PP = 5,10,15,20\text{-tetra}(p\text{-methoxyphenyl})porphyrinato$ dianion; dppe = diphenylphosphinoethane).

All calculations were performed with the Amsterdam Density Functional (ADF) program from Scientific Computing and Modeling (SCM; Netherlands).[22,23] A TZ2P basis of Slater orbitals was employed for all calculations. The geometry optimizations used medium size effective core potentials and the GGA:BLYP XC functional. The spectral calculations (done at the optimized geometries) employed the SOAP[24] model XC potential and used the Davidson Method[25,26] to determine the low lying excited states and oscillator strengths.

Simultaneous Chronoabsorptometry and Chronoamperometry of Ferrocene. Visible-NIR data were collected under anaerobic (dinitrogen atmosphere) conditions using an Ocean-Optics USB 2000 detector (360−1000 nm), an Ocean Optics LS-1-tungsten lamp, and a T-300-dip-probe. The absorbance spectrum of a 5.59 mM solution of ferrocene in 0.10 M NBu_4PF_6/MeCN was recorded using the same concentration of a blank support electrolyte solution as reference. The path length was 1.00 cm.

The fiber-optic spectroelectrochemical cell configuration was near-identical to the one previously described for mid-IR experiments.[12] Specifically, the light from the dip probe was directed through 2−3 mm of a solution of ferrocene (ca. 3.0 mM) in 0.10 M NBu_4PF_6/MeCN onto a polished 3.0 mm BAS Pt electrode. This configuration allows the beam to reflect off of the electrode back into the T-300-dip-probe and to the detector. A Pt wire was used as the auxiliary electrode. For MeCN solutions, a bare Ag wire was used as a quasi-reference electrode; for other solvents, a Ag wire electrocoated with AgCl was used as the reference electrode. The Ocean Optics OOIBASE or Spectrasuite program was set to record and save spectra automatically upon receiving trigger signals (external software trigger). A 10−15 ms integration time was used.

(11) Shaw, M. J.; Geiger, W. E. *Organometallics* **1996**, *15*, 13–15.
(12) Shaw, M. J.; Henson, R. L.; Houk, S. E.; Westhoff, J. W.; Jones, M. W.; Richter-Addo, G. B. *J. Electroanal. Chem.* **2002**, *534*, 47–53.
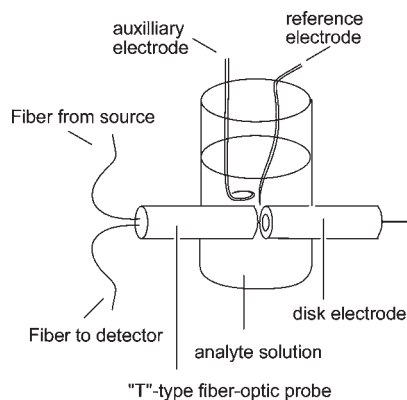(13) Shaw, M. J.; Afridi, S. J.; Light, S. L.; Mertz, J. N.; Ripperda, S. E. *Organometallics* **2004**, *23*, 2778–2783.
(14) Carter, S. M.; Lee, J.; Hixson, C. A.; Powell, D. R.; Wheeler, R. A.; Shaw, M. J.; Richter-Addo, G. B. *Dalton Trans.* **2006**, 1338–1346.
(15) Zahran, Z. N.; Shaw, M. J.; Khan, M. A.; Richter-Addo, G. B. *Inorg. Chem.* **2006**, *45*, 2661–2668.
(16) Shriver, D. F.; Drezdzon, M. A. *The Manipulation of Air-Sensitive Compounds*, 2nd ed.; Wiley-Interscience: Toronto, 1986.
(17) Wayda, A. L.; Darensbourg, M. Y. *Experimental Organometallic Chemistry: A Practicum in Synthesis and Characterization*; American Chemical Society: Washington, D.C., 1987.
(18) Adler, A. D.; Longo, F. R.; Finarelli, J. D.; Goldmacher, J.; Assour, J.; Korsakoff, L. *J. Org. Chem.* **1967**, *32*, 476.
(19) Adler, A. D.; Longo, F. R.; Kampas, F.; Kim, J. *J. Inorg. Nucl. Chem.* **1970**, *32*, 2443–2445.
(20) Richter-Addo, G. B.; Hodge, S. J.; Yi, G.-B.; Khan, M. A.; Ma, T.; Caemelbecke, E. V.; Guo, N.; Kadish, K. M. *Inorg. Chem.* **1996**, *35*, 6530–6538 [Erratum: 1997, p 2696].
(21) Bond, A. M.; Grabaric, B. S.; Grabaric, Z. *Inorg. Chem.* **1978**, *17*, 1013–1018.
(22) te Velde, G.; Bickelhaupt, F. M.; van Gisbergen, S. J. A.; Fonseca Guerra, C.; Baerends, E. J.; Snijders, J. G.; Zeigler, T. *J. Comput. Chem.* **2001**, *22*, 931–967.
(23) Baerends, E. J.; Autschbach, J.; Bashford, D.; Bérces, A.; Bickelhaupt, F. M.; Bo, C.; Boerrigter, P. M.; Cavallo, L.; Chong, D. P.; Deng, L.; Dickson, R. M.; Ellis, D. E.; van Faassen, M.; Fan, L.; Fischer, T. H.; Fonseca Guerra, C.; Ghysels, A.; Giammona, A.; van Gisbergen, S. J. A.; Gotz, A. W.; Groeneveld, J. A.; Gritsenko, O. V.; Grüning, M.; Harris, F. E.; van den Hoek, P.; Jacob, C. R.; Jacobsen, H.; Jensen, L.; van Kessel, G.; Kootstra, F.; Krykunov, M. V.; van Lenthe, E.; McCormack, D. A.; Michalak, A.; Mitoraj, M.; Neugebauer, J.; Nicu, V. P.; Noodleman, L.; Osinga, V. P.; Patchkovskii, S.; Philipsen, P. H. T.; Post, D.; Pye, C. C.; Ravenek, W.; Rodriguez, J. I.; Ros, P.; Schipper, P. R. T.; Schreckenbach, G.; Seth, M.; Snijders, J. G.; Sola, M.; Swart, M.; Swerhone, D.; te Velde, G.; Vernooijs, P.; Versluis, L.; Visscher, L.; Visser, O.; Wang, F.; Wesolowski, T. A.; van Wezenbeek, E.; Wiesenekker, G.; Wolff, S. K.; Woo, T. K.; Yakolev, A. L.; Ziegler, T. http://www.scm.com; Vrijie Universiteit: Amsterdam, The Netherlands, 2009.
(24) Gritsenko, O. V.; Schipper, P. R. T.; Baerends, E. J. *Chem. Phys. Lett.* **1999**, *302*, 199–207.
(25) van Gisbergen, S. J. A.; Snijders, J. G.; Baerends, E. J. *Comput. Phys. Commun.* **1999**, *118*, 119–138.
(26) Wang, F.; Ziegler, T. *Mol. Phys.* **2004**, *102*, 2585–2595.

Figure 1. Schematic representation of the spectroelectrochemical cell (analyte volume of ~15 mL). A photo of the cell is supplied in the Supporting Information, Figure S1.

A Labview 8.0 program was written to control a National Instruments USB-6251 interface so as to apply a potential to the working electrode via the external input of an EG&G PAR 263A potentiostat, to record the current and potential analog output of the potentiostat, and to apply digital trigger signals at regular known intervals to the USB-2000 detector. Labview programs developed for these application are posted on the National Instruments Developer Zone Web site (http://decibel. ni.com/content/people/roadchem?view=documents; accessed 9/1/10). In these experiments, the data collection rate was typically set to 500 Hz, the potential was set either 100 or 300 mV positive of ferrocene's E° value (as determined by an initial cyclic voltammogram), and 20 spectra were recorded at 0.200−0.500 s intervals. The files and the current versus time data were saved for subsequent processing.

A second Labview 8.0 program was written which performs an optional "edge correction" on the current versus time data to account for radial-edge diffusion at the electrode.[27] The current−time data was corrected, then integrated, and the charges that corresponded to times when the spectra were recorded were noted. At every wavelength used to construct the spectrum, a linear least-squares analysis was performed which yielded a slope that was then converted to an absorptivity (extinction coefficient) value. The standard deviation of each absorptivity at each wavelength was also calculated.

Measurements on (T(p-OMe)PP)Co, (T(p-OMe)PP)Co(NO), and (dppe)Mn(CO)$_3$Br. Beer's Law plots of these complexes were obtained using a 1.0 cm cuvette held in an Ocean-Optics CUV-ALL-UV 4-way Cuvette Holder, using an Ocean-Optics USB 4000 fiber-optic spectrophotometer (200−850 nm) and a LS-1 tungsten lamp. Simultaneous chronoabsorptometry/chronoamperometry measurements were performed as described above, but employing the spectroelectrochemical cell sketched in Figure 1 and shown in Supporting Information, Figure S1. This cell was custom-made by Chemglass (www.chemglass.com), and assigned part numbers SIUE-0803−041MS (cell body, specify closed bottom) and SIUE-0803−042MS (cell cap).

Electron Paramagnetic Resonance (EPR) Spectroscopy. A commercial EPR spectroelectrochemical cell (Wilmad) was used for in situ EPR spectroscopic measurements. Typically, a 1.0 M solution of analyte in 0.5 M NBu$_4$PF$_6$ in CH$_2$Cl$_2$ was injected into the cell in a drybox. The electrodes were positioned, and the cell sealed and secured in the EPR cavity. A potential sufficient to cause current to flow through the cell was applied, and an EPR spectrum was recorded.

Electrochemical Data Processing and Methodology. For the redox reaction shown in eq 1, the integrated Cottrell equation (eq 2)[28] describes the

$$A + ne^- \rightleftharpoons B \tag{1}$$

$$Q = 2nFA_e C_A^* \sqrt{\frac{Dt}{\pi}} + Q_{dl} + nFA_e\Gamma_A \tag{2}$$

chronocoulometric charge that flows through an electrode as a function of time after a potential is applied. This equation results from the application of the Nernst equation and Fick's laws of diffusion to a planar electrode where linear diffusion is the only means by which redox-active material is transported to the electrode surface.[29] The applied potential has to be such that virtually all of the material that diffuses to the electrode surface undergoes electron transfer on contact. In eq 2, the charge (Q) is expressed as a function of time (t), the number of electrons (n), Faraday's constant (F), the electrode area (A_e), the diffusion coefficient of the species present in the bulk solution (D), and the concentration of the redox species in the bulk solution which undergoes electron transfer (e.g., C_A^* for species A). Q also depends on a term due to adsorbed surface species ($nFA_e\Gamma_A$, where Γ_A is the fraction of the surface covered) and double layer charging (Q_{dl}). For species that do not adsorb to the electrode surface, the values of $nFA_e\Gamma_A$ and Q_{dl} are very small, and these processes are often complete within 50 ms of the application of the pulse.[30−32]

Equation 3 shows the relationship of the absorbance ($Abs_{B(\lambda,t)}$) of species B generated at an electrode surface with time, assuming that the values of D for the various species present are similar.[28] This equation is the basis of chronoabsorptometry at wavelengths where the starting material does not interfere.

$$Abs_{B(\lambda,t)} = 2\varepsilon_{B(\lambda)} C_A^* \sqrt{\frac{Dt}{\pi}} \tag{3}$$

A similar equation can also be derived for the variation in the starting material's absorbance with time. If adsorption and double layer charging are small, these two equations can be combined with eq 2 to yield eq 4 (see Supporting Information).

$$\Delta Abs_{(\lambda,t)} = \frac{Q}{nFA_e}(\varepsilon_{B(\lambda)} - \varepsilon_{A(\lambda)}) \tag{4}$$

Equation 4 shows how the change in absorbance ($\Delta Abs_{(\lambda,t)}$) in a set of difference spectra varies with the charge Q passed through the electrode. From eq 4, it is evident that a plot of change in absorbance versus charge at any specific wavelength for a set of difference spectra should yield a straight line with slope of $(\varepsilon_{B(\lambda)} - \varepsilon_{A(\lambda)})/nFA_e$. Thus, if $\varepsilon_{A(\lambda)}$, n, and A_e are known, then the value of $\varepsilon_{B(\lambda)}$ can be extracted. This calculation may be repeated at each wavelength to obtain the complete absorptivity versus wavelength spectrum of the redox product. This approach renders quantitative information about electrode products for reactions which exhibit complete chemical reversibility, or complete chemical irreversibility.

Absorptivity information is also available for electrode reactions that exhibit *partial* chemical reversibility. Consideration of the chronoabsorptometry equations for an *EC* electrode mechanism (eq 5) with a first order or pseudo-first order chemical

(27) Heinze, J. *J. Electroanal. Chem.* **1981**, *124*, 73–86.

(28) Kissinger, P. T.; Heineman, W. R. In *Laboratory Techniques in Electroanalytical Chemistry*, 2nd ed. (revised and expanded); Kissinger, P. T., Heineman, W. R., Eds.; Marcel Dekker, Inc: New York, 1996; pp 57−68.

(29) Bard, A. J.; Faulkner, L. R. *Electrochemical Methods: Fundamentals and Applications*, 2nd ed.; Wiley: New York, 2001.

(30) Schwarz, W. M.; Shain, I. *J. Phys. Chem.-Us* **1965**, *69*, 30–40.

(31) Christie, J. H.; Osteryoung, R. A.; Anson, F. C. *J. Electroanal. Chem.* **1967**, *13*, 236–244.

(32) Anson, F. C.; Osteryoung, R. A. *J. Chem. Educ.* **1983**, *60*, 293–296.

step yields eq 6 (derived in Supporting Information). The $\gamma_{(k_i',t)}$ function (eq 7) describes

$$A + ne^- \rightleftharpoons B \xrightarrow{k_f} C \qquad (5)$$

$$\frac{\Delta Abs_{(\lambda)}}{Q} = \frac{\gamma_{(k_f',t)}}{nFA_e}(\varepsilon_{B(\lambda)} - \varepsilon_{C(\lambda)}) + \frac{1}{nFA_e}(\varepsilon_{C(\lambda)} - \varepsilon_{A(\lambda)}) \qquad (6)$$

$$\gamma_{(k_f',t)} = e^{-k_f't} \sum_{n=0}^{\infty} \frac{(k_f't)^n}{(2n+1)n!} \qquad (7)$$

the variation of species B and C with time. Since $\gamma_{(k_i',t)}$ converges within a few terms (10 iterations are convenient), it can be easily calculated. Rate constants k_f' can be obtained by voltammetry. From eq 6, it can be deduced that plots of $(\Delta Abs_{(\lambda)})/Q$ versus $\gamma_{(k_i',t)}$ should yield linear plots where the slope gives the difference between the absorptivity of the intermediate B and the product C, and the intercept yields the difference between the absorptivity of the product C and the starting material A. Thus, if the starting material's absorptivity is known, then the values of $\varepsilon_{C(\lambda)}$ and $\varepsilon_{B(\lambda)}$ can be obtained from the intercept and slope, respectively, when both are multiplied by nFA_e. Repetition at each wavelength should then yield complete absorptivity versus wavelength curves for the intermediate and product. However, it is important to note that the quality of the final data depends on the quality of the ε_λ values known for the starting material since the method relies on *differences* in absorptivity. Thus, a Beer's Law plot of the starting material should be performed to ascertain absorptivity values in the concentration range where data collection is performed, and the spectroelectrochemistry of compounds with non-linear Beer's law plots should be approached with caution.

Results and Discussion

We demonstrate the use of new spectroelectrochemical methodology employing simultaneous chronoabsorptometry and chronoamperometry for the facile detection of unstable redox products not previously detected by current spectroelectrochemical methods. This section is divided into two parts: (i) development of the method and proof-of-concept using the well-studied ferrocene/ferrocenium couple and application to the detection of a porphyrin π-radical cation, and (ii) application of the method to generate and characterize, for the first time, an unstable intermediate in a redox-induced *fac* to *mer* reaction pathway for a coordination compound of manganese.

Proof of Concept. The methodology employed in this work is based on established electrochemical principles. The theory[33,34] and application[35,36] of chronoabsorptometry have been reported. In our continuing efforts to improve the spectroelectrochemical methodology for the ready generation and detection of reaction intermediates, we have employed the fundamental mathematics of chronoabsorptometry to develop readily accessible instrumentation to generate UV−vis absorption spectra of intermediates not observable by current techniques that employ OTTLE or other spectroelectrochemical cells. The advantages of this new methodology (e.g., using

eqs 4 and 6) include the following: (i) there is no *arbitrary* spectral subtraction of the starting material's spectral features to enhance the spectrum of the intermediate, (ii) the approach is independent of knowledge of the accurate path length of the electrochemical cell, and (iii) quantitative knowledge of the absorptivity values facilitates assignment of the spectra features for the electrode species. In previous work by others, an approach using eq 4 was applied by measuring $\varepsilon_{B(\lambda)}$ values one at a time over a given spectral window;[35,36] this approach proved to be quite tedious, requiring > 60 manual trials at each separate λ. To the best of our knowledge, eq 6 has not been used previously to yield absorptivity versus wavelength data from a single experiment. Given the current availability of inexpensive diode-array-detector-based fiber-optic spectrometers, fast analog/digital I/O devices, and fast computers, it is now possible to use techniques based on these equations to generate the UV−vis spectrum of a product generated at an electrode surface during a chronoabsorptometric experiment at multiple wavelengths simultaneously.

The electrochemical cell is simple in design and is sketched in Figure 1 (see also Supporting Information, Figures S1 and S2). In this configuration, a waveguide brings light through the analyte solution to and from the electrode surface, and provision is made for stirring. The final equation utilized in this proof-of-concept demonstration is given by eq 4 (Experimental Section, and see Supporting Information for derivation).[35] Note that this eq 4 does not include terms for concentration or path length as variables;

$$\Delta A_{(\lambda,t)} = \frac{Q}{nFA_e}(\varepsilon_{B(\lambda)} - \varepsilon_{A(\lambda)}) \qquad (4)$$

these terms, however, are needed for the determination of the required Beer's law plots (see later).

Ferrocene. We chose ferrocene (Cp$_2$Fe; Cp = (η^5-C$_5$H$_5$), cyclopentadienyl) as the prototype to demonstrate this method as it is known to undergo a well-characterized one-electron oxidation in various solvents (eq 8),[37−39] and is a widely accepted electrochemical redox standard.[2]

$$Cp_2Fe \rightleftharpoons [Cp_2Fe]^+ + e^- \qquad (8)$$
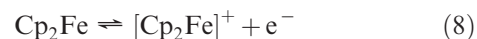
Importantly, the UV−vis spectra of authentic samples of the neutral ferrocene and its oxidized derivative of eq 8 have been reported previously.[40,41]

Figure 2 shows the final plots of absorptivity (ε) versus wavelength for both Cp$_2$Fe and [Cp$_2$Fe]$^+$ in acetonitrile obtained from this work; the sample was kept under rigorously anaerobic conditions so as to avoid follow-up reactions with oxygen. The spectrum for the starting Cp$_2$Fe compound was obtained from Beer's law plots, while that for [Cp$_2$Fe]$^+$ was obtained after a four-second data collection experiment using our new methodology (from 20 spectra; each 15 ms integration time at 0.2 s

(33) Li, C.-Y.; Wilson, G. S. *Anal. Chem.* **1973**, *45*, 2370–2380.
(34) Evans, D. H.; Kelly, M. J. *Anal. Chem.* **1982**, *54*, 1727–1729.
(35) Jones, D. H.; Hinman, A. S. *Can. J. Chem.* **1996**, *74*, 1403–1408.
(36) Jones, D. H.; Hinman, A. S. *Can. J. Chem.* **2000**, *78*, 1318–1324.
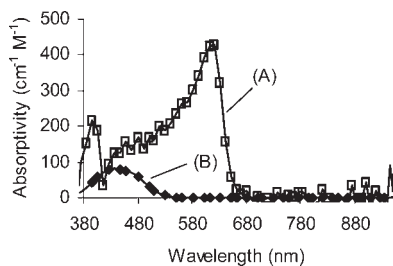
(37) Tsierkezos, N. G. *J. Solution Chem.* **2007**, *36*, 289–302.
(38) Crooks, R. M.; Bard, A. J. *J. Electroanal. Chem.* **1988**, *243*, 117–131.
(39) Kadish, K. M.; Ding, J. Q.; Malinski, T. *Anal. Chem.* **1984**, *56*, 1741–1744.
(40) Prins, R. *J. Chem. Soc. D: Chem. Commun.* **1970**, 280b–281.
(41) Scott, D. R.; Becker, R. S. *J. Organomet. Chem.* **1965**, *4*, 409–411.

Figure 2. Plots of absorptivity versus wavelength for (A) ferrocenium ion (□) generated at an electrode surface over a four-second period from electrooxidation of 3.4 mM ferrocene in 0.10 M NBu_4PF_6/MeCN at 298 K, and (B) ferrocene (◆).

intervals). Notably, the value of λ_{max} at 619 nm and associated absorptivity of $450\ cm^{-1}$ are similar to reported literature values.[40,41] The processes involved in computing the spectrum for $[Cp_2Fe]^+$ are shown schematically in Figure 3. We used chronoamperometry (Figure 3A,B) to determine the current response as a function of time, and the plot obtained was as expected from the Cottrell equation. Simultaneously, spectra were collected every 0.2 s in the 380–800 nm range along the decay curve for the data shown in Figure 3B; in general, however, we sampled every 0.5 s for the Co and Mn systems (see later). Correction for edge diffusion for small electrodes is necessary to obtain accurate values of Q by integration of current data.[19] To perform edge correction for chronoamperometry, we applied the method of Heinze (Supporting Information, Figure S3)[27] noting the near-perfect fit of the correction factor to eq S24 (see Supporting Information). The edge correction requirement introduces two readily obtained variables into the experiment, namely, the geometric radius of the electrode (easily obtained) and the diffusion coefficient of the compound being studied (e.g., $D°$ (ferrocene) $= 2.24 \times 10^{-5}\ cm^2\ s^{-1}$;[37,39] can be extracted from chronoamperometry data collected during the experiment). From Figure 3B and the edge correction data, we obtained values of Q by integration (note that $I = Q/t$) along the decay trace.

A resulting plot of change in total absorbance (i.e., for starting material and product; see eqs S1–S10 in the Supporting Information) versus corrected Q for a representative λ is shown in Figure 3C; similar plots are determined for each λ sampled (i.e., > 2500 separate wavelength measurements). From eq 4 and Figure 3C, the slope is given by $\Delta\varepsilon_\lambda/nFA_e$ for a particular λ, where $\Delta\varepsilon_\lambda$ is equal to $\varepsilon_\lambda(B) - \varepsilon_\lambda(A)$.

Thus, the value of $\varepsilon_\lambda(B)$ (i.e., absorptivity of product at a particular wavelength) can be obtained from knowledge of the slope of the line in Figure 3C ($\Delta\varepsilon_\lambda/nFA_e$; if the electrode area (A_e) and number of electrons (n) are known) and by calculating $\Delta\varepsilon_\lambda(A)$ of the starting compound using Beer's law. Importantly, the computer analysis of the data collected after this 4 s experimental run to give the spectrum of $[Cp_2Fe]^+$ shown in Figure 2 is obtained in < 1 s on a standard modern computer! We noted previously that the final eq 4 used was independent of concentration and path length. Thus, there is no need for the reproducible placement of the electrode(s) and waveguide with respect to each other. Indeed, we find that we obtain good reproducibility for the value of $\varepsilon_\lambda(B)$ (to within 6%) even if (i) the electrode area is assumed
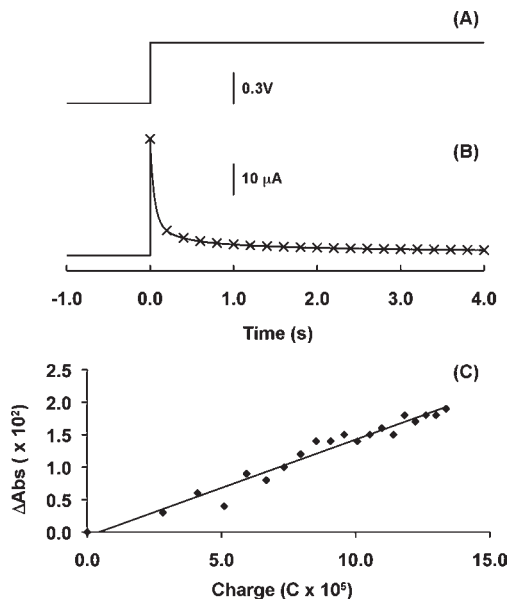
Figure 3. (A) Potential versus time for a typical chronoamperometry/chronoabsorptometry experiment. (B) Current response versus time recorded during the potential step shown for 3.9 mM ferrocene in 0.1 M NBu_4PF_6. Times at which spectra were recorded are indicated by ×'s. (C) Change in absorbance vs charge recorded at 619 nm (◆) with least-squares best fit (solid line). Charge was obtained by integration of current after applying a correction for radial diffusion as described by Heinze (See Supporting Information, Figure S3).[19]

constant over multiple experiments (i.e., if we did not redetermine the exact value of electrode area), (ii) we did not fix the concentrations of analytes to be the same over the trials, and (iii) we did not take special precautions to keep the path length identical over several runs. We find that larger deviations occur where the spectrometer has lower sensitivity (i.e., < 400 nm and > 900 nm) mostly because of the emission characteristics of the tungsten halide source, and that brief stirring (e.g., for 15 s) between runs is necessary to ensure reproducibility.

In summary, we have used the ferrocene-ferrocenium couple to demonstrate a robust calculation of absorptivity over a range of wavelengths for electrogenerated products at an electrode surface. The four-second experimental time frame is comparable to many cyclic voltammetry time scales, and the spectra obtained are essentially independent of path length and concentration. Further, the method is simple, reliable with no ambiguity over the exact value of applied potential (c.f. the OTTLE cell limitation), and yields quantitative spectral information on electrode products.

Cobalt Nitrosyl Porphyrins. The electrochemistry of cobalt nitrosyl porphyrins has been reported; these compounds undergo multiple electron transfer events.[20,42−45] The square-wave voltammogram for the oxidation of (T(*p*-OMe)PP)Co(NO) is shown in Figure 4A, and reveals

(42) Kelly, S.; Lançon, D.; Kadish, K. M. *Inorg. Chem.* **1984**, *23*, 1451–1458.

(43) Kadish, K. M.; Mu, X. H.; Lin, X. Q. *Inorg. Chem.* **1988**, *27*, 1489–1492.

(44) Kini, A. D.; Washington, J.; Kubiak, C. P.; Morimoto, B. H. *Inorg. Chem.* **1996**, *35*, 6904–6906.

(45) Kadish, K. M.; Ou, Z.; Tan, X.; Boschi, T.; Monti, D.; Fares, V.; Tagliatesta, P. *J. Chem. Soc., Dalton Trans.* **1999**, 1595–1601.
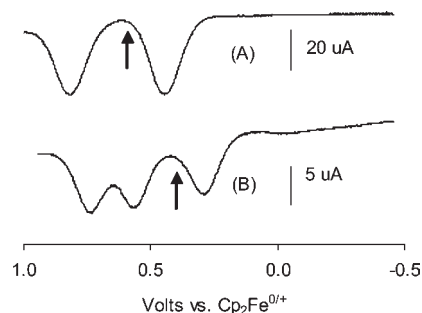
Figure 4. Square wave voltammograms of (A) 0.22 mM (T(*p*-OMe)-PP)Co(NO) and (B) 0.13 mM (T(*p*-OMe)PP)Co in CH$_2$Cl$_2$/0.1 M NBu$_4$PF$_6$ at 298 K. Arrows indicate the potentials applied for the chronoamperometry/chronoabsorptometry method used to obtain spectroscopic data. Scan parameters: 2 mV pulse width, 50 mV pulse height, 50 Hz.

redox processes at $E^{o\prime}$ = 0.46 and 0.84 V versus the Fc/Fc$^+$ couple consistent with that reported previously for this compound.[20,44] For comparison, the square-wave voltammogram of the parent (T(*p*-OMe)Co compound is shown in Figure 4B, with $E^{o\prime}$ values of 0.31, 0.59, and 0.75 V versus the Fc/Fc$^+$ couple.

The ~150 mV positive shift of the first oxidation of (T(*p*-OMe)PP)Co(NO) relative to that of (T(*p*-OMe)-PP)Co is not unexpected, and this magnitude of shift has been observed for other cobalt nitrosyl porphyrins as well.[43,45]

We were interested in the product of the first oxidation of (T(*p*-OMe)PP)Co(NO) (eq 9; site of oxidation not indicated) to better define the location of electron

$$(\text{T}(p\text{-OMe})\text{PP})\text{Co(NO)} \rightleftharpoons [(\text{T}(p\text{-OMe})\text{PP})\text{Co(NO)}]^+ + e^-$$

$$(9)$$
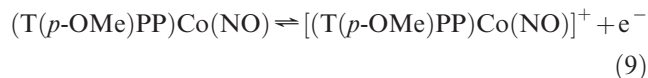
removal (e.g., metal- or porphyrin-based oxidation) on the short time-scales now available to us. Using the procedures described in the previous section, we obtained plots of ε versus λ for the product obtained after the first oxidation (Figure 5). The electrode was set at a potential just positive of the first oxidation couple for the cobalt complex in Figure 4A (at +0.6 V versus the ferrocene-ferrocenium couple). The diffusion coefficients used to perform the edge correction for (T(*p*-OMe)PP)Co(NO) and (T(*p*-OMe)PP)Co were found to be 1.15×10^{-5} cm^2 s^{-1} and 1.33×10^{-5} cm^2 s^{-1}, respectively. The resulting plot is shown in Figure 5A and is compared with that of the parent neutral (T(*p*-OMe)PP)Co(NO).

The neutral (T(*p*-OMe)PP)Co(NO) displays a Soret band at 420 nm and a visible band at 541 nm ($\varepsilon = 1.95 \times 10^4$ M^{-1} cm^{-1}). The oxidized product shows the presence of a new absorption band centered at 658 nm ($\varepsilon = 3.2 \times 10^4$ M^{-1} cm^{-1}). This new band is attributed to the formation of the [(T(*p*-OMe)PP•$^+$)Co(NO)] π-radical cation species at the electrode surface (eq 10), as this band is in the ~600–700 nm region generally associated with tetraarylporphyrin

(46) Gross, Z.; Barzilay, C. *Angew. Chem., Int. Ed. Engl.* **1992**, *31*, 1615–1617.
(47) Fuhrhop, J.-H. *Struct. Bonding* (*Berlin*) **1974**, *18*, 1–67.
(48) Fujita, E.; Chang, C. K.; Fajer, J. *J. Am. Chem. Soc.* **1985**, *107*, 7665–7669.
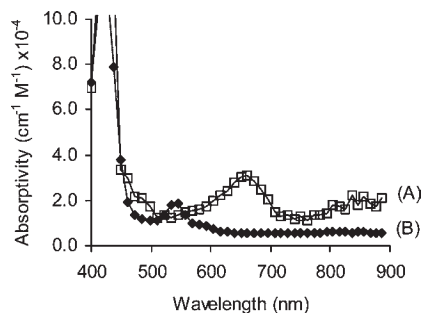
Figure 5. Absorptivity vs wavelength for (A) [(T(*p*-OMe)PP)Co(NO)]$^+$ (□), generated at an electrode surface over a 10 s period from 0.22 mM (T(*p*-OMe)PP)Co(NO) in 0.10 M NBu$_4$PF$_6$/MeCN at 298 K, and (B) (T(*p*-OMe)PP)Co(NO) (◆).

π-radical cations.[46,47] The related [(OEP•$^+$)Co(NO)] is known to display visible bands in the 520–570 nm region.[48]

$$(\text{T}(p\text{-OMe})\text{PP})\text{Co(NO)} \rightleftharpoons [(\text{T}(p\text{-OMe})\text{PP}•^+)\text{Co(NO)}] + e^-$$

$$(10)$$
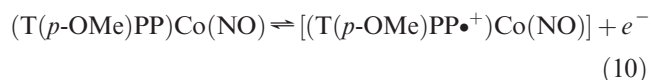
In contrast, the absorptivity plot of the non-nitrosyl-containing (T(*p*-OMe)PP)Co compound does not show a new band at ~650 nm upon oxidation (Supporting Information, Figure S4). The absence of this feature is consistent with (T(*p*-OMe)PP)Co undergoing a metal-based oxidation rather than a porphyrin-based oxidation under our conditions (eq 11).[43]

$$(\text{T}(p\text{-OMe})\text{PP})\text{Co}^{II} \rightleftharpoons [(\text{T}(p\text{-OMe})\text{PP})\text{Co}^{III}]^+ + e^-$$

$$(11)$$
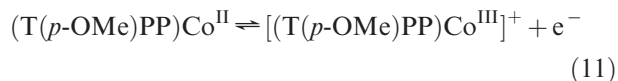
Taken together, the results of eqs 10 and 11 are consistent with similar results published for other cobalt porphyrin compounds.[20,42,43,45] However, the spectral information obtained in Figure 5A for the [(T(*p*-OMe)PP•$^+$)Co(NO)] π-radical cation from this short time scale absorptivity method *avoids spectral contamination* from byproducts generated at 298 K when longer time scales are utilized.

To demonstrate the effects of longer time scales and the effects of thin-layer resistance on the integrity of the initially generated (T(*p*-OMe)PP•$^+$)Co(NO) compound, we used in situ EPR spectroelectrochemical methodology employing a commercial air-free sample cell. We note that Kadish and co-workers have reported the in situ EPR spectrum of the oxidation product of the related (TPP)Co(NO) complex in dichloromethane,[43] without obvious side-products. The 293 K EPR spectrum of the oxidation product of (T(*p*-OMe)PP)Co(NO), electrogenerated in an air-free commercial thin-layer EPR cell, is shown in Figure 6A; the analogous spectrum of electrogenerated [(T(*p*-OMe)PP)Co]$^+$ is shown in Figure 6B. As can be deduced from a comparison of these spectra, the longer time scales (up to 600 s) typically utilized in the EPR spectroelectrochemistry experiments can result in the unwanted loss of the NO fragment from the singly oxidized derivative of the cobalt nitrosyl porphyrin to give [(T(*p*-OMe)PP)Co^{III}]$^+$. Such a loss of the NO fragment has been described by Kadish and co-workers for other (por)Co(NO) compounds.[20,42,43,45]

In summary, although the first oxidation product of (T(*p*-OMe)PP)Co(NO) has been proposed to be the
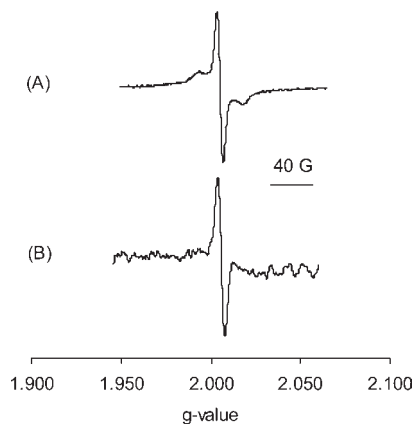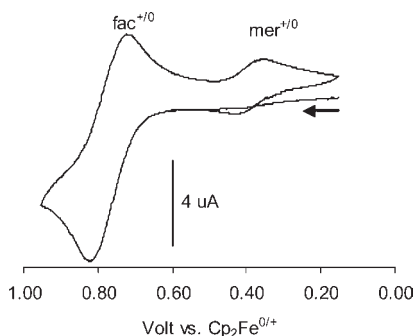
Figure 6. X-Band EPR spectra of the oxidized products of (A) (T(*p*-OMe)-PP)Co(NO) and (B) (T(*p*-OMe)PP)Co, generated by electrochemical in situ oxidation in 0.5 M NBu_4PF_6/CH_2Cl_2 at 293 K. The top figure shows spectral contamination by the species in (B).

Figure 7. Cyclic voltammogram of 1.0 mM *fac*-[(dppe)Mn(CO)$_3$Br] in 0.1 M NBu_4PF_6/CH_2Cl_2 at 0.40 V/s and 298 K. Arrow indicates initial direction of scan. Note the reversibility of the *mer*$^{+/0}$ feature revealed upon the subsequent scan.

π radical cation [(T(*p*-OMe)PP•$^+$)Co(NO)] on the basis of IR spectroscopy,[20,44] this work confirms its assignment by UV−vis spectroscopy. The successful demonstration of the use of the simultaneous chronoamperometry/chronoabsorptometry to provide proof-of-concept for the determination of UV−vis spectra of redox products at an electrode surface allowed us to use this method to determine the UV−vis spectrum of an intermediate which has never before been characterized.

Application for the Detection of Electrode Intermediates. The compound *fac*-[(dppe)Mn(CO)$_3$Br] (referred to herein as *fac*) contains a Mn-tricarbonyl moiety in a facial arrangement. Such *fac*-[(L$_2$)Mn(CO)$_3$Br] (L$_2$ = chelating diphosphines/bipyridines) are known to undergo *fac* to *mer* isomerization reactions following oxidation.[21] These reactions are of renewed interest because structural changes that follow electron-transfer reactions are of fundamental importance to applications such as long-term digital memory storage.

We thus chose the *fac*-[(dppe)Mn(CO)$_3$Br] compound as our prototype for the study of *redox-induced* configurational lability in transition metal complexes. The cyclic voltammogram of *fac*-[(dppe)Mn(CO)$_3$Br] is shown in Figure 7.

The compound undergoes a well-behaved one-electron oxidation process with scan rate-dependent chemical reversibility, consistent with the formation of the oxidation

$$fac \underset{}{\overset{E°_{(fac)}}{\rightleftharpoons}} fac^+ \xrightarrow{k} mer^+$$

Figure 8. EC mechanism for the oxidation of *fac*-[(dppe)Mn(CO)$_3$Br] which results in the formation of the *mer*-[(dppe)Mn(CO)$_3$Br]$^+$ cation.
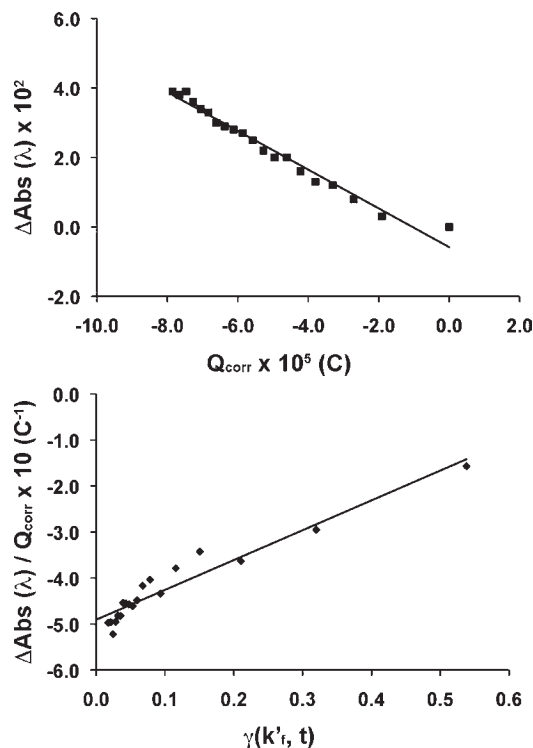

Figure 9. (A) Change in absorbance data recorded at 517 nm during the simultaneous chronoamperometry/chronoabsorptometry experiment plotted versus corrected charge (Q_{corr}) as developed in "method 1" (R^2 = 0.9739). (B) Change in absorbance divided by Q_{corr}, plotted against the dimensionless parameter $\gamma(k'_f, t)$ as defined in "method 2" (R^2 = 0.9229).

product *fac*$^+$. This initially generated species converts to a daughter product that shows a redox feature at a less positive potential. These CV features are consistent with isomerization of *fac*$^+$ to the corresponding *mer*$^+$ as detailed in Figure 8.[21]

A value of *k* of 1.5 s^{-1} for the *fac*$^+$ → *mer*$^+$ step in acetonitrile was determined previously by Bond using chronoamperometry;[21] a similar value of 2.0 s^{-1} for this process in CH_2Cl_2/NBu_4PF_6 was determined by us by digital simulation (DigiElch) of background-subtracted square wave voltammetry data.

Importantly, the scan rate-dependent chemical reversibility of the process *fac* → *fac*$^+$ → *mer*$^+$ implies the existence of more than two species at the electrode surface (i.e., a classic *EC* electrode mechanism). Thus, although the absorptivity method described in the previous section can give information on the absorptivity of *mer*$^+$, it is not entirely appropriate for this particular sequence of reactions because it does not take into account the time-dependent absorbance of the additional species on the electrode surface. The solution to this issue is fortunately straightforward. The data collection strategy is exactly the same as that described in the previous (proof-of-concept) section, but the analysis of the data is performed according to eq 6 for the EC case (c.f., eq 4). In eq 6, ε_A, ε_B,
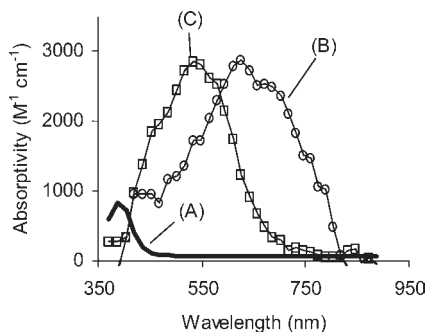
Figure 10. Absorptivity versus wavelength for (A) *fac*-[(dppe)Mn(CO)₃Br] (solid line), (B) *fac*-[(dppe)Mn(CO)₃Br]$^+$ (○) with data smoothed using a median filter, and (C) *mer*-[(dppe)Mn(CO)₃Br]$^+$ (□). The cationic species were generated at an electrode surface over a 10 s period from 1.0 mM *fac*-[(dppe)Mn(CO)₃Br] in 0.10 M NBu₄PF₆/CH₂Cl₂ at 298 K. It is possible that the low energy shoulders in trace (B) may be artifacts of curve smoothing. See the Supporting Information for the raw spectral data for (B) prior to smoothing.

and ε_C represent the absorptivities of *fac*, *fac*$^+$, and *mer*$^+$, respectively.

$$\frac{\Delta Abs_{(\lambda)}}{Q} = \frac{\gamma_{(k_{f'}, t)}}{nFA_e}(\varepsilon_{B(\lambda)} - \varepsilon_{C(\lambda)}) + \frac{1}{nFA_e}(\varepsilon_{C(\lambda)} - \varepsilon_{A(\lambda)}) \tag{6}$$

This equation takes into consideration the absorbance of an intermediate generated at the electrode surface. A plot of $\Delta Abs_\lambda/Q$ (i.e., the change in total absorbance at a given wavelength divided by the corrected charge) versus $\gamma(k, t)$, where t represents the time at which the spectrum was taken, yields a straight line with an intercept of $(\varepsilon(C)_\lambda - \varepsilon(A)_\lambda)/nFA_e$ (Figure 9). From the value of this intercept, and with $\varepsilon(A)_\lambda$ known, we can extract the absorptivity of species C (*mer*$^+$) without it being contaminated by the presence of other species. The diffusion coefficient of *fac* used for the correction of radial diffusion was determined to be 1.09×10^{-5} cm² s^{-1} by chronoamperometry.

A unique advantage of this method is that it allows, for the first time, the recovery of information about B (*fac*$^+$) from the slope of the line in Figure 9 so that we can unambiguously characterize it spectrally although it may be present only in very low concentration. Figure 10 shows the plots of ε versus λ for species A (*fac*), B (*fac*$^+$), and C (*mer*$^+$). The spectra for species C (λ_{max} 540 nm; $\varepsilon = 2.8 \times 10^3$ M^{-1} cm^{-1}) match the spectra reported by others ($\varepsilon_{540} = 2.1 \times 10^3$ M^{-1} cm^{-1}).[21] The spectrum for A (λ_{max} 395 nm; $\varepsilon_{395} = 6.8 \times 10^2$ M^{-1} cm^{-1}), however, differs from that previously reported (λ_{max} 388 nm; $\varepsilon_{388} = 1.3 \times 10^3$ M^{-1} cm^{-1}). However, the latter literature values were obtained using a 2 mM solution in a 1.0 mm OTTLE cell.[41] The ε_{395} value for *fac*-[Br(CO)₃(dppe)Mn] obtained in this work results from a Beer's law plot ($R^2 = 0.997$) of five different concentrations for solutions prepared in a drybox in volumetric glassware measured using a calibrated 1.00 cm quartz cuvette.

Returning to Figure 10, we note that the UV–vis spectral characterization of B has, however, never been reported previously despite numerous studies of the processes described by Figure 8 using OTTLE spectroelectrochemical cells (note that the use of OTTLE cells generally requires
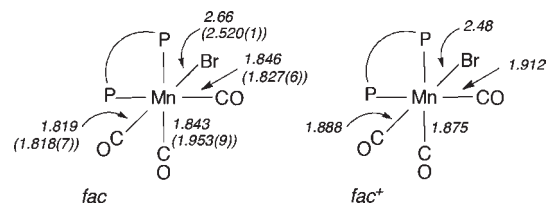
Figure 11. Geometry-optimized structures of *fac* and *fac*$^+$ from DFT calculations. The data in brackets are from the experimental crystal structure.[50]

longer time scales (≥ 30 s) for data collection). The EPR spectrum of the related *fac*-[(dppm)Mn(CO)₃Cl]$^+$ (dppm = 1,1-bis(diphenylphosphino)methane) has been reported by Bond;[49] this cation was generated from nitrosonium oxidation at low temperature of the neutral precursor in acetonitrile, under conditions where the sample temperature was briefly raised to 202 K and refreezing the sample to 77 K. The optical method described herein is expected to yield complementary solution-phase information to such low-temperature frozen glass EPR studies.

The correct calculation of the spectrum of B (λ_{max} 623 nm; $\varepsilon = 2.9 \times 10^3$ M^{-1} cm^{-1}) in Figure 10 requires knowledge of the rate constant k for the *fac*$^+$ to *mer*$^+$ isomerization process; plots of the effects of different arbitrary values of k on the shape of this spectrum are shown in Supporting Information, Figure S5. This data has been smoothed with a median filter, the effect of which can be seen by comparing Supporting Information, Figures S6 and S7. We find from our DFT calculations (next section) that the λ_{max} and absorptivity values for the *fac*$^+$ cation are consistent with the smaller gap between the highest occupied molecular orbital (HOMO) and the lowest unoccupied molecular orbital (LUMO) expected relative to either the neutral *fac* or the cationic *mer*$^+$ complexes.

Theoretical Calculations. To verify our spectral assignment for the *fac*$^+$ intermediate, we performed density functional theory (DFT) calculations to obtain optimized geometries for the four species *fac*, *fac*$^+$, *mer*$^+$, and *mer* (see the Supporting Information, Table S1 and Figures S12–S15). The geometry optimization of *fac* is in close agreement with the geometrical data obtained for this compound from a single-crystal X-ray structural analysis reported previously (Figure 11).[50] The X-ray crystal structure of *mer*$^+$ has not been reported.

The computational results of the *fac*$^+$ species were of particular interest to us. Single-point calculations on the geometry-optimized structures reveal that the energy of the *fac*$^+$ species is 151.4 kcal/mol above that of the *fac* species, and 4.6 kcal/mol above that of the isomerized *mer*$^+$ species. The HOMO of the starting *fac* compound is shown in Figure 12. It can be seen from this Figure that the HOMO comprises contributions from a Mn–Br antibonding interaction and a Mn–CO bonding interaction. Thus, upon oxidation, the Mn–Br bond is expected to become stronger and the Mn–CO bonds weaker. This is, in fact, borne out by the bond distance changes obtained

(49) Bond, A. M.; Colton, R.; Mccormick, M. J. *Inorg. Chem.* **1977**, *16*, 155–159.

(50) Beckett, M. A.; Brassington, D. S.; Coles, S. J.; Gelbrich, T.; Light, M. E.; Hursthouse, M. B. *J. Organomet. Chem.* **2003**, *688*, 174–180.
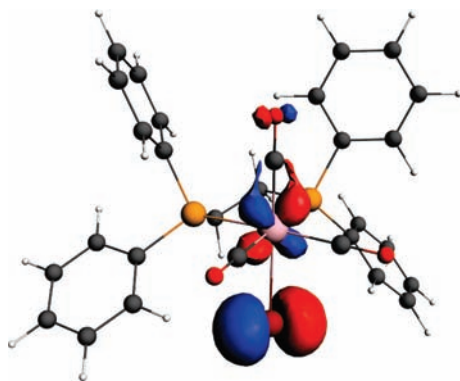
Figure 12. HOMO of *fac*-(dppe)Mn(CO)$_3$Br.

Table 1. Experimental and Calculated λ_{max} Values for [(dppe)Mn(CO)$_3$Br]$^{0/+}$

species	experimental λ_{max} (nm)[a]	calculated λ_{max} (nm)[b]
fac-[(dppe)Mn(CO)$_3$Br]	395	398
mer-[(dppe)Mn(CO)$_3$Br]	418, 455 (sh)[c]	424, 446[d]
fac-[(dppe)Mn(CO)$_3$Br]$^+$	650	623
mer-[(dppe)Mn(CO)$_3$Br]$^+$	456 (sh), 564	442, 540

[a] CH$_2$Cl$_2$/0.1 M NBu$_4$PF$_6$, 298 K. [b] 50 nm peak widths assigned. [c] Estimated from reference 21 (Figure 4 therein). [d] Calculated with 20 nm peak width.

from the DFT calculations on the oxidized *fac*$^+$ species as shown in Figure 11.

We then performed time dependent DFT (TD-DFT) calculations to obtain the predicted spectra of the *fac* and *mer* isomers of both the neutral and the cationic [(dppe)Mn(CO)$_3$Br] complexes to obtain an independent measure of the quality of the *fac*-[(dppe)Mn(CO)$_3$Br]$^+$ spectrum determined from the simultaneous chronoamperometry/chronoabsorptometry method. The calculated spectra for these species are displayed in Supporting Information, Figures S8–S11. Importantly, the calculated UV–vis spectra λ_{max} values for the *fac*, *mer*$^+$, and *mer* compounds match those determined experimentally to within ±27 nm.[41] The calculated spectrum for *fac*$^+$ also matches that obtained by application of eq 6 and shown in Figure 10.

The LUMO of neutral *fac*-[Br(CO)$_3$(dppe)Mn] complex was found to be predominantly d$_{z^2}$ in character (Supporting Information, Figure S16). Both the HOMO and the LUMO are essentially unchanged in *fac*$^+$. The HOMO (Supporting Information, Figure S17) and LUMO (Supporting Information, Figure S18) of *mer*$^+$ are predominantly d$_{xz}$ and d$_{yz}$ respectively, with significant contributions from the p orbitals of Br. Isomerization of *fac*$^+$ to

mer$^+$ increases the HOMO–LUMO gap. Thus, λ_{max} for the short-lived *fac*$^+$ intermediate is expected to occur at longer wavelengths than either the starting material (Figure 10C) or the final product (Figure 10A).

For the easily observed neutral 18-electron species, the calculated λ_{max} values are within 9 nm of the experimental values (Table 1).[21,51] The 17-electron *mer*$^+$ cation is also easily observed by UV–vis methods, and its calculated λ_{max} values are within 24 nm of experiment. This larger variation is acceptable because the open-shell configuration of the cation introduces more complexity to the calculation. The calculations reproduce the single peak expected for the neutral *fac* species and the two peaks observed for both *mer* species. The excellent agreement between the spectra and the calculations for the three previously observed species suggests that the calculated λ_{max} value for *fac*$^+$ is also valid. The calculated and experimental values for *fac*$^+$ obtained from our work agree to within 27 nm, so these results serve to validate the method used to obtain and smooth the spectrum of the short-lived cationic *fac*$^+$ complex.

Conclusions

We have developed a rapid and efficient approach using simultaneous chronoamperometry and chronoabsorptometry to obtain UV–vis spectral data on intermediates generated on electrode surfaces under normal cyclic voltammetry time scales (0.05–1.5 V/s). We have demonstrated its applicability for the generation of hitherto unreported spectra for the short-lived *fac*-[(dppe)Mn(CO)$_3$Br]$^+$ intermediate that forms during the redox-induced *fac*→*mer* isomerization of (dppe)Mn(CO)$_3$Br. The instrumentation is relatively inexpensive. The absorptivities measured by the simultaneous chronoabsorptometry/chronoamperometry methodology are essentially independent of path length and of the concentration of the starting material. The method extracts absorptivity information on the short-lived intermediates using proven mathematical relationships.

Supporting Information Available: Derivations of equations, definitions, additional figures (electrochemical cell, absorptivity plots, calculated geometries and spectra, molecular orbital pictures). This material is available free of charge via the Internet at http://pubs.acs.org.

(51) Pereira, C.; Ferreira, H. G.; Schultz, M. S.; Milanez, J.; Izidoro, M.; Leme, P. C.; Santos, R. H. A.; Gambardella, M. R. P.; Castellano, E. E.; Lima-Neto, B. S.; Carlos, R. M. *Inorg. Chim. Acta* **2005**, *358*, 3735–3744.